Radio Science, Volume ???, Number , Pages 1–32,

First two years of TanDEM-X mission: interferometric performance overview

Michele Martone,[1] Paola Rizzoli,[1] Benjamin Bräutigam,[1] and Gerhard Krieger[1]

Corresponding author: Michele Martone, Microwave and Radar Institute, German Aerospace Center (DLR), Münchner Straße, 20, 82234, Weßling, Germany. (Michele.Martone@dlr.de)

[1]Microwaves and Radar Institute,
German Aerospace Center (DLR),
Oberpfaffenhofen, Germany.

The TanDEM-X mission (TerraSAR-X add-on for Digital Elevation Measurement) comprises two nearly identical satellites: TerraSAR-X (TSX, launched in June 2007), and TanDEM-X (TDX, launched in June 2010), which form an innovative and flexible single-pass radar interferometer. The primary objective of the mission is to generate a worldwide and consistent digital elevation model (DEM) with an unprecedented accuracy. After a calibration phase of the TDX satellite, which was performed during the first three months after its launch, the two satellites were brought into close formation to begin the bistatic commissioning phase. Then, in December 2010, TanDEM-X started the operational global DEM acquisition in bistatic configuration. During the last two years, dedicated analyses on test acquisitions as well as persistent monitoring of the interferometric performance have been carried out, which are the subject of this paper. Key quantities in estimating interferometric performance such as coherence, relative height error, and phase unwrapping indicators are investigated, showing the outstanding capabilities of TanDEM-X. Then, the main focus is shifted to those critical areas which, for various reasons, have shown unsatisfactory data quality, and therefore must to be reacquired with optimized imaging geometries in order to fulfill the DEM accuracy requirements. Promising results have been obtained so far, and future strategies to handle the critical data are discussed. This paper will present an overview of the interferometric performance of TanDEM-X, based on investigations performed in the first two years of mission oper-

ation, and includes results from the bistatic commissioning phase until the end of the first global DEM acquisition.

1. Introduction

Digital elevation models (DEMs) are presently widely employed in many commercial and scientific applications, such as Geographic Information Systems and the Global Positioning System (GPS), as well as in geoscience fields, e.g. geology, physical geography, glaciology, and oceanography. For such applications, DEMs are exploited for the estimation and assessment of several geophysical parameters, such as ground deformations and Earth's topography [*Moreira et al.*, 2004], [*Zebker et al.*, 1994]. In 2000, the Shuttle Radar Topography Mission (SRTM) created the first near-global data set of land elevations (for latitudes between -56° and $+60^\circ$) [*Farr et al.*, 2007]. Since then, an increasing interest for more accurate interferometric products covering the entire land mass has arisen in the scientific community as well as among commercial customers. The TanDEM-X mission (TerraSAR-X add-on for Digital Elevation Measurement) is the first operational spaceborne bistatic SAR system which comprises two nearly identical SAR satellites: TerraSAR-X (TSX, launched in June 2007) and TanDEM-X (TDX, launched in June 2010). Like the TerraSAR-X mission, TanDEM-X is a project developed under a public-private partnership between the German Aerospace Center (DLR) and Astrium GmbH [*Werninghaus and Buckreuss*, 2010], [*Buckreuss and Schättler*, 2010]. The primary objective of the mission is to generate a worldwide and consistent DEM with an unprecedented accuracy [*Krieger et al.*, 2007]. To do so, at least two global mappings of the Earth's landmass will be performed and, in order to keep the performance nearly constant over range, mutually displaced beams will be used. Additionally, the employment of different baselines will

allow to further improve the unwrapping process and DEM quality [*Lachaise et al.*, 2007]. Flying in a close orbit configuration, the TSX and TDX satellites act as a large single-pass radar interferometer, overcoming the limitations inherent in repeat-pass interferometry, such as temporal decorrelation, and allowing for the acquisition of highly accurate cross- and along-track interferograms [*Krieger et al.*, 2007]. In Table 1, the DEM specifications for the SRTM [*Rodriguez et al.*, 2006] and TanDEM-X [*Wessel*, 2013] missions are shown and compared. During the first three months after its launch, the TDX satellite was tested and calibrated in monostatic configuration with the two satellites flying at 20 km along-track distance. It was proven that the system performance of TDX is very similar to that of TSX [*Kraus et al.*, 2011], [*Schwerdt et al.*, 2012]. On the 14^{th} of October, 2010, both satellites were brought into close formation, at a few hundred meters of distance [*Bachmann and Hoffmann*, 2010]. Since then, acquisitions are operationally performed in bistatic configuration: either TSX or TDX is employed for transmission and both satellites simultaneously record the signal, which is backscattered from the Earth's surface to both radar antennas. Then, in December 2010, TanDEM-X started the nominal global DEM acquisition. In order to ensure the quality of the final DEM, a very accurate calibration of the bistatic system and of the interferometric baseline was required [*Hueso González et al. ISPRS*, 2012]. After about two years of nominal mission operation, more than 300,000 bistatic scenes (of 30 km x 50 km size) have been produced for performance assessment by the Interferometric TanDEM-X Processor [*Fritz et al.*, 2011], showing that TanDEM-X is able to provide the remote

sensing scientific community with a unique data set to be exploited for a wide range of commercial and scientific applications. More information about the distribution of TanDEM-X data to the scientific community can be found in [*TanDEM-X Science Server*, 2010].

In this paper, an overview of the interferometric performance of TanDEM-X is presented, based on the experience of the first two years of mission operation, going from the bistatic commissioning phase until the end of the first global DEM acquisition. Statistical results of key quantities in estimating interferometric performance, such as coherence and phase unwrapping indicators, are shown, and the current status of global DEM acquisition is presented in the next section. A relative height error verification approach, by means of repeated acquisitions on defined test-sites, is provided in Section 3. Section 4 presents performance results over critical areas and consequent actions taken in the acquisition plan. Forested areas show additional coherence degradation due to the presence of volume scattering, and implications on the global acquisition strategy are described as well. Then, possible scenarios to cope with those regions characterized by rugged topography are discussed. Regions severely affected by the so-called SNR decorrelation, which occurs when only a limited part of the radar signal is backscattered to the receiving antenna, are investigated, and a solution is proposed to minimize the performance loss.

2. Interferometric Performance Statistics

One of the key parameters for the evaluation of interferometric performance is the coherence γ. It represents the normalized correlation coefficient between master (u_1) and slave (u_2) acquisition, and its absolute value gives information about the amount of noise in the interferogram. Coherence is given by [*Zebker and Villasenor*, 1992], [*Bamler and Hartl*, 1998]

$$\gamma = \frac{\mathrm{E}[u_1 u_2^*]}{\sqrt{\mathrm{E}[|u_1|^2][|u_2|^2]}}. \quad (1)$$

Several error sources may contribute to coherence loss [*Krieger et al.*, 2007], [*Martone et al., ISPRS*, 2012]. The knowledge of the coherence and of the independent number of looks n employed within the multilooking process allows for the estimation of the interferometric phase error φ, whose probability density function (pdf) can be expressed as [*Lee et al.*, 1994]

$$p_\varphi(\varphi) = \frac{\Gamma(n+\frac{1}{2})(1-\gamma^2)^n\,\gamma\,cos\varphi}{2\sqrt{\pi}\Gamma(n)(1-\gamma^2\,cos^2\varphi)^{n+\frac{1}{2}}} + \frac{(1-\gamma^2)^n}{2\pi} F\left(n, 1; \frac{1}{2}; \gamma^2\,cos^2\varphi\right), \quad (2)$$

where Γ is the gamma function and F is the hypergeometric function [*Abramowitz and Stagun*, 1965].

The relative vertical accuracy of a DEM is defined as the difference between two independent height estimates (point-to-point height error), which is due to the fluctuation of the interferometric phase at each location. From a statistical standpoint, the computation of the difference between two random variables corresponds to the convolution between the two pdfs $p_\varphi(\varphi)$. The 90% point-to-point phase error $\Delta\varphi_{90\%}$

can be then derived from

$$\int_{-\Delta\varphi_{90\%}}^{\Delta\varphi_{90\%}} [p_\varphi(\varphi) * p_\varphi(\varphi)]\,\mathrm{d}\varphi = 0.9, \tag{3}$$

where the symbol $*$ denotes convolution. From the estimated $\Delta\varphi_{90\%}$, the 90% point-to-point relative height error, as required by the TanDEM-X DEM specifications [*Wessel*, 2013], may be finally expressed as

$$\Delta h_{90\%} = \mathrm{HoA} \cdot (\Delta\varphi_{90\%}/2\pi)\,. \tag{4}$$

HoA stands for height of ambiguity, which represents the height difference corresponding to a complete 2π cycle of the interferometric phase and, in turn, is defined as

$$\mathrm{HoA} = \frac{\lambda r \sin(\theta_i)}{\mathrm{B}_\perp}, \tag{5}$$

where λ is the radar wavelength, r is the slant range, θ_i is the incidence angle, and $B_\perp$ is the baseline perpendicular to the line of sight (also referred to as "effective" baseline).

2.1. Commissioning Phase

The bistatic commissioning phase started on the 14^{th} of October, 2010 and ended on the 12^{th} of December, 2010, at which time TanDEM-X began the nominal DEM acquisition. During the bistatic commissioning phase, more than 4,400 bistatic scenes were processed and evaluated. Each scene has a typical extension of 50 km by 30 km in azimuth and range, respectively. Several tests were carried out to analyse the performance for the full range of acquisition parameters. For each processed scene, the mean coherence over land has been recorded. A water mask of about

300 m x 300 m resolution [*GLOBCOVER*, 2009] was used to exclude large water bodies which are typically characterized by low coherence. The histogram in Figure 1 represents the coherence distribution of the acquisitions performed during the bistatic commissioning phase. The mean value is approximately 0.71 and in more than 80% of the cases the observed coherence is higher than 0.6. For acquisition geometries typical for the TanDEM-X mission, a coherence around 0.6 still provides, in most cases, a sufficient unwrapping quality [*Krieger et al.*, 2007], [*Martone et al., ISPRS*, 2012]. The investigated test acquisitions were uniformly distributed from the land cover point of view, in order to get a quality assessment of the data over many possible land cover scenarios. During this period, a relative big and constant helix was employed [*Krieger et al.*, 2007], with an horizontal distance between the two satellites of about 350 m, and a vertical distance of about 400 m. Consequently, a wide range of height of ambiguities was exploited, and particularly small values were obtained at the Equator by using steep incidence angles. Statistics about phase unwrapping quality indicators, e.g., residues and branch cuts, have been evaluated as well. The residues are related to phase gradient estimation errors and identify, in the interferogram, the endpoints of lines along which the true phase gradient exceeds $\pm\pi$. These lines are called branch-cuts [*Zebker and Lu*, 1998], [*Bamler and Hartl*, 1998]. A quality indicator has been set to flag scenes with more than 1% residue [*Suchandt and Eineder*, 2003] (which means that 1% of the pixels of a scene are affected), and from the commissioning phase data, a mean percentage of 0.98% was observed; for single branch cuts, the average percentage per scene is about 0.81%. Considering

the excellent results obtained during the bistatic commissioning phase, the nominal DEM acquisition phase could proceed without restrictions, and statistical results are presented in the next subsection.

2.2. Global DEM Acquisition

TanDEM-X nominal DEM acquisition was started on 12^{th} December 2010. From that day on, TSX and TDX acquired more than 220,000 bistatic scenes (until the end of December 2012). Up to now, TanDEM-X has completed the first global DEM for latitudes greater than $-60°$, with heights of ambiguity typically ranging between 45 m and 50 m. The second coverage has been completed in mid 2013, with a desired HoA of about 35 m [*Krieger et al.*, 2007], [*Ortega-Míguez et al.*, 2012]. The combination of all available acquisitions by means of multi-baseline phase unwrapping algorithms will then allow to fully meet the DEM specification requirements [*Lachaise et al.*, 2007]. Figure 2 gives a view of the distribution of the mean interferometric coherence per scene provided by the first global coverage (the Antarctic region will be processed in a later mission phase). The obtained mean coherence over all scenes is approximately 0.76. In particular, more than 91% of the processed DEM scenes are characterized by a mean land coherence higher than 0.6, and 47% are even higher than 0.8. Very good performance is shown by phase unwrapping quality indicators as well: the mean percentage of single cuts and phase residues are around 0.65% and 0.73%, respectively, which indicates that the phase unwrapping quality is already sufficient for many scenes without using a second acquisition in combination with dual baseline phase unwrapping [*Suchandt and Eineder*, 2003]. Looking at the acquisitions from the

second global coverage available so far, a substantial stability in terms of performance has been observed, which verifies the outstanding capabilities and the interferometric product quality of TanDEM-X.

3. Relative Height Error Analysis

The relative height error is the uncertainty due to noise-like disturbance contributions, which affects the relative vertical accuracy of a DEM [*Wessel*, 2013]. It is proportional to the height of ambiguity and to the interferometric phase error (as expressed in (2)). The specification for the TanDEM-X mission is a 90% point-to-point error of 2 m and 4 m for areas with predominant slope less than 20% and greater than 20%, respectively (see Table 1).

From a statistical point of view, it has been demonstrated in [*Rizzoli et al. ISPRS*, 2012] that the point-to-point (pp) relative height error can be reasonably approximated by a normal distribution with zero mean and standard deviation σ_h

$$\Delta h_{pp} \sim \mathcal{N}(0, {\sigma_h}^2). \tag{6}$$

A statistical description of the point-to-point interferometric phase error is given by linear transformation of Δh_{pp} (according to (4))

$$\Delta \varphi_{pp} = \frac{2\pi}{\mathrm{HoA}} \Delta h_{pp}. \tag{7}$$

Hence, the interferometric phase error is also normally distributed and can be expressed as

$$\Delta \varphi_{pp} \sim \mathcal{N}(0, {\sigma_\varphi}^2). \tag{8}$$

where

$${\sigma_\varphi}^2 = \left[\frac{2\pi}{\mathrm{HoA}}\right]^2 {\sigma_h}^2. \tag{9}$$

According to (6), the 90% point-to-point relative height error $\Delta h_{90\%}$ may be derived from

$$\mathrm{erf}\left(\frac{\Delta h_{90\%}}{\sqrt{2}\sigma_h}\right) = 0.9, \tag{10}$$

where $\mathrm{erf}(\cdot)$ is the Gauss error function, defined as

$$\mathrm{erf}(x) = \frac{1}{\sqrt{\pi}} \int_{-x}^{x} e^{-t^2} \mathrm{d}t. \tag{11}$$

For a quantitative assessment of the TanDEM-X performance, the relative height error is derived from the interferometric coherence [*Krieger et al.*, 2007], [*Lee et al.*, 1994]. In particular, for each pixel of a processed interferogram, the 90% relative height error, $\Delta h_{90\%}$, is estimated (see also Section 2). From the resulting height error map, the mean value per scene is then considered for statistics. In order to validate the described procedure, the relative height accuracy has been derived from TanDEM-X data by means of repeated acquisitions over defined test sites. The workflow followed for the present investigation is shown in Figure 3: the DEM difference is evaluated from two repeated DEM acquisitions (with identical acquisition geometry and configuration). Due to a baseline estimation error of about 1 mm [*Antony et al.*, 2013], the resulting DEM horizontal localization accuracy (for typical TanDEM-X baselines and incidence angles) is in the order of a few meters [*Hueso González et al. IGARSS*, 2012], [*Hueso González et al. ISPRS*, 2012]. Then, a high-pass filtering is performed to erase slowly-varying error contributions, such as orbit or attitude uncertainties, which will be likewise removed during the final DEM calibration process. In this way, a matrix of relative height error values is estimated. In order to discriminate between flat and mountainous areas, a slope mask, generated from the

gradient matrix of one of the two DEMs, is then applied to the height error map [*Rizzoli et al. ISPRS*, 2012]. On the top-left side of Figure 4 the coherence map for one bistatic acquisition over the Death Valley is shown. Death Valley is located in Eastern California and is a very dry and rocky region, characterized by the presence of both flat and mountainous topography. According to Figure 3, the DEM difference from two repeated acquisitions is calculated (top-right of Figure 4). It is worth pointing out that the individual TanDEM-X DEM scenes delivered by the Interferometric TanDEM-X Processor are only roughly calibrated [*Fritz et al.*, 2011], [*Rossi et al.*, 2012], which explains the almost constant offset of about 3 m observed between the two DEMs. Such residual biases and offsets are subject to the final calibration and mosaicking, which is performed by a second independent processing system, the Mosaicking and Calibration Processor (MCP) [*Gruber et al.*, 2012], [*Huber et al.*, 2012]. Then, a high-pass filter is applied (in frequency domain) to the obtained DEM difference matrix in order to include only the noise-like error contributions. Finally, the histogram of the absolute value of the point-to-point relative height error is calculated (Figure 4, bottom), and the resulting 90^{th} percentile is about 2.3 m. The 90% height error for areas with slopes smaller and greater than 20% are indicated as well. A detailed description about the height error estimation approach, and results from relative height error analysis by means of repeated TanDEM-X acquisitions can be found in [*Rizzoli et al. ISPRS*, 2012]. In Table 2 the acquisition parameters for the two repeated data-takes are listed, and the 90% point-to-point relative height error estimated from the coherence is about 2.2 m. A good agreement between the two

height error estimation approaches has been verified, with a deviation of about 10 cm. It has been furthermore demonstrated [*Rizzoli et al. ISPRS*, 2012] that the results from the relative height error analysis match very well with the theoretical DEM performance derived in [*Krieger et al.*, 2007], verifying that TanDEM-X performs as expected. Starting from these preconditions, a global assessment of the relative vertical accuracy can be performed. In Figure 5, the global 90% point-to-point relative height error map for the first DEM acquisition is depicted, estimated from the global coherence map of Figure 2 according to (4). In Figure 6, the distribution of the estimates is shown: it can be observed that more than 25% of the land masses show a 90% point-to-point relative height error smaller than 1.8 m (leaving 20 cm as residual error budget). For these areas, a single acquisition is already sufficient in order to achieve the final 2 m specification. Nevertheless, they have also been included in the acquisition plan for the the second global coverage to further enhance the overall DEM performance in terms of height accuracy and phase unwrapping quality. On the other hand, several areas, represented in yellow and red in Figure 5, require multiple interferometric acquisitions in order to reduce the relative height error (this topic is discussed in the next section). Furthermore, the opportunity of using TanDEM-X quicklook data for global performance statistics and monitoring in order to achieve a much finer spatial resolution (in the order of few hundred of meters) is currently being investigated [*Rizzoli et al. EuSAR*, 2012].

4. Performance Analysis and Acquisition Strategies over Critical Areas

4.1. Forested Areas

In vegetated areas, volume scattering is an important source of coherence loss [*Treuhaft and Siqueira*, 2000]: the existence of multiple scatterers at different heights and within a single resolution cell results in an increase of the interferometric phase uncertainty. In order to monitor volume decorrelation effects, test acquisitions over areas with different vegetation characteristics were performed. As an example, Figure 7 shows the coherence maps for two bistatic acquisitions over the same area in the Amazon rainforest. For each scene, the incidence angle (θ_{inc}), the effective baseline ($B_{\perp}$) and the height of ambiguity (HoA) are indicated. For the image on the left, the height of ambiguity is 25 m, for the one on the right it is 52 m. The improvement is particularly visible over the forested areas (lower part of the image), whereas for the clear-cut areas almost the same performance is obtained. Figure 8 shows the measured coherence for the Amazon rainforest as a function of the height of ambiguity for a large set of acquisitions from the nominal DEM phase. As it can be seen from the figure, the specific acquisition geometry plays a key-role in interferometric performance for scenes acquired in presence of strong volume decorrelation phenomena. Because of this, the desired height of ambiguity for the first global DEM acquisitions (depicted in red) was changed from 40 m (as initially set) to 45 m. Furthermore, in order to improve the phase unwrapping quality, a dedicated mission phase has been reserved to reacquire densely forested areas using smaller baselines (i.e. higher HoA). To accomplish this, the TanDEM-X acquisition plan was consequently adapted, and

the order of helix satellite formations [*Krieger et al.*, 2007] was reversed, starting with larger baselines, and gradually reducing them in order to reacquire affected data with an improved imaging geometry [*Bachmann et al.*, 2012]. The obtained coherence is depicted in Figure 8 (green dots). For heights of ambiguity larger than 55 m, a coherence above 0.6 is usually obtained, and the mean coherence improvement with respect to the first global DEM acquisitions is approximately 16%. In general, volume decorrelation effects have been observed over areas characterized by different forest types, such as rainforests, tropical as well as boreal forests. Even stronger coherence loss is obtained if a dense forest is combined with a hilly or mountainous topography, which is discussed in the next section. However, one has to be aware that the height of ambiguity is directly proportional to the relative height error accuracy, as shown in (2), and should be kept small in order to meet the height accuracy requirements. On the other hand, it could be verified that the interferometric coherence of areas characterized by soil and rock show only a slight dependency on the height of ambiguity.

4.2. Mountainous Regions

Several error contributions occur in radar imagery over areas characterized by pronounced topography. Baseline (often referred to as "geometrical") decorrelation is similar to the effect occurring in the presence of volume scattering. It is caused when imaging a flat surface from slightly different incidence angles [*Li and Goldstein*, 1990] and can be mitigated by filtering the two range spectra to a common frequency interval [*Gatelli et al.*, 1994]. Nevertheless, steep and irregular surfaces are more susceptible to phase-unwrapping errors, and the resulting DEM accuracy is inevitably affected. Figure 9 shows the coherence maps for two bistatic acquisitions over the the Mount Cayambe in the Ecuadorian Andes. For each scene, the acquisition parameters are indicated and in particular, the image on the left has a height of ambiguity of 48 m, where for the image on the right it is 77 m. As a result of the mitigation of baseline decorrelation effects, a mean coherence improvement of about 9% is observed. For both acquisitions, the satellites fly in ascending orbit and operate in right-looking geometry. The image on the right, however, still presents phase instabilities due to residual baseline decorrelation (the effective baseline is inversely proportional to the relative vertical accuracy, as shown in (3), and can not be reduced as required). A significant enhancement of the phase unwrapping quality is obtained by the combination of both acquisitions through multi-baseline phase unwrapping algorithms [*Lachaise et al.*, 2007], [*Lachaise et al.*, 2012]. Therefore, together with forested areas (as discussed in Section 4.1), mountainous regions have been systematically reacquired with a more suitable imaging geometry. Neverthe-

less, many low coherence areas remain, mainly consisting of slopes facing the radar (layover), or away from the antenna illumination (shadow). The coherence maps for two acquisitions performed with different orbit direction over the Cayambe volcano are shown in Figure 10. The region common to both scenes is outlined in red. For each scene, layover and shadow have been estimated by exploiting amplitude and coherence information, and are highlighted with different colors. In particular, layover occurs when different object points have the same azimuth and range time and, therefore, are mapped into one image pixel. For layover, the received backscattered power is high, but, due to the dominant baseline decorrelation, a very low coherence (i.e., $\gamma < 0.3$) is typically observed. Shadow is the region where an object point is not reached by any radar beam. It is independent from the backscatter of the terrain and corresponds to "missing" data inside the image. From comparing the two scenes in Figure 10, it can be seen that several pixels are detected as either shadow or layover in only one of the two images. In general, an opportune combination of scenes acquired with different geometries would lead to a mitigation of such distortions, resulting in a better reconstruction of the illuminated area. The remaining shadow and layover after the combination of the two acquisitions are depicted in pink in Figure 11, and correspond to those pixels which are affected in both images. In the present example, more than 70% of shadow and layover occurring in the ascending orbit (left-hand side of Figure 10) acquisition and 50% of shadow and layover affecting the descending orbit (right-hand side of Figure 10) acquisition, could be resolved. For TanDEM-X, nominal DEM acquisitions are performed in ascending orbit over the northern hemi-

sphere, and in descending orbit over the southern hemisphere. In order to mitigate these geometric distortions and to improve the overall accuracy of the final DEM, additional coverages of mountainous areas with inverted orbit direction (and heights of ambiguity larger than 60 m) will be executed in a dedicated mission phase [*Borla Tridon et al.*, 2013].

4.3. Low Backscatter Areas

In interferometric SAR applications, the finite sensitivity of the receiving system represents a significant error source. The corresponding coherence loss is given by [*Just and Bamler*, 1994], [*Zebker and Villasenor*, 1992]

$$\gamma_{\mathrm{SNR}} = \frac{1}{\sqrt{1+\mathrm{SNR}_{\mathrm{TSX}}^{-1}} \cdot \sqrt{1+\mathrm{SNR}_{\mathrm{TDX}}^{-1}}}, \tag{12}$$

where $\mathrm{SNR}_{\mathrm{TSX,TDX}}$ is the signal-to-noise ratio of the two satellites. The SNR is a measure that describes the image quality of a SAR system, estimating how much the radar signal has been corrupted by noise. It depends on the backscatter coefficient (σ_0) and the noise equivalent sigma zero (NESZ), which accounts for the system noise contributions, e.g. antenna pattern, instrument thermal noise, and processing filters. The observed difference in terms of SNR between TSX and TDX is quite small (usually less than 1 dB) and, therefore, it can be reasonably assumed that $\mathrm{SNR}_{\mathrm{TSX}} = \mathrm{SNR}_{\mathrm{TDX}} = \mathrm{SNR}$. Dedicated investigations have shown that for most of the land cover types an SNR below 7 dB is rarely obtained, providing quite stable interferometric performance ($\gamma_{\mathrm{SNR}} > 0.83$) and good phase unwrapping quality [*Martone et al., IGARSS*, 2012]. On the other hand, in Figure 12, the coherence maps of two bistatic scenes over the Taklamakan desert, located in North-West China, are shown. For the image on the left side, the incidence angle is approximately 43°, for the one on the right side it is about 26°. The estimated SNR is up to 6 dB higher for the image acquired with a steeper incidence angle, and a coherence improvement of about 60% (from 0.44 to 0.71) is obtained over the areas covered by sand. Over the rocky region (in the central part of the images) similar performance is observed. In

Figure 13, the mean coherence against incidence angle is shown for test acquisitions over four desert regions located in different areas the world. The weak backscattered power considerably affects the performance over sandy deserts, and strongly depends on the acquisition geometry. For typical incidence angles of TanDEM-X nominal mission operation (ranging between 30° and 48°), a coherence above 0.5 is rarely observed (corresponding to SNR smaller than 2 dB [1]). Based on these promising results, a reacquisition of regions showing weak backscatter will be performed after the completion of the second global coverage using steeper incidence angles, in order to minimize the performance loss.

5. Conclusions

TanDEM-X is the first operational spaceborne bistatic SAR system comprising two independent satellites. This paper presents an overview of interferometric performance after two years of mission operation. Statistical results from the bistatic commissioning phase and nominal DEM acquisitions verify outstanding interferometric capabilities and data quality. In particular, from the first global DEM, a good phase unwrapping quality has been obtained for different land cover scenarios. An interferometric coherence higher than 0.6 has been observed for more than 90% of the acquired scenes, and 25% of them already fulfill the DEM accuracy specification after one single acquisition. The use of TanDEM-X quicklook data for global performance statistics and monitoring allows to achieve a much finer spatial resolution, and is currently being investigated. For the second global coverage (ended on mid 2013) a different acquisition geometry and slightly displaced beams have been employed, to further improve the phase unwrapping stability and the final DEM accuracy. In general, good and consistent performance has been obtained so far, proving that TanDEM-X is able to provide the remote sensing scientific community with a unique global data set with an unprecedented accuracy, and to apply innovative techniques for many commercial and scientific applications, as well as for the design of future missions. A procedure for the estimation of the relative height error from TanDEM-X repeated acquisitions has been discussed, and the approach to quantitatively calculate the relative height accuracy from interferometric data has been shown and verified. Areas affected by different decorrelation sources were investigated in

detail. In particular, phase uncertainty over densely forested areas increases due to the presence of volume scattering, and a similar mechanism (the so-called baseline decorrelation) is responsible for performance loss over mountainous regions. A reacquisition of these critical areas has been performed with smaller baselines, leading to a significant improvement of the phase unwrapping stability and corresponding DEM accuracy. Moreover, areas characterized by rugged topography will be additionally imaged with inverted orbit direction in order to mitigate geometrical distortions, such as shadow and layover. Over sandy deserts the image quality is severely affected by SNR decorrelation. In order to minimize performance loss, the acquisition of such areas will be repeated by employing steeper incidence angles, made possible by exploiting the high flexibility of TanDEM-X.

401 **Acknowledgments.** The authors would like to thank C. Wecklich from DLR for
402 his help and assistance. The authors would like to thank the anonymous reviewers
403 for their valuable comments and suggestions that helped to improve this paper. The
404 TanDEM-X project is partly funded by the German Federal Ministry for Economics
405 and Technology (Förderkennzeichen 50 EE 1035).

Notes

1. According to (4), an SNR of about 0 dB should be obtained for $\gamma = 0.5$. However, other error sources (as, e.g., ambiguities or coregistration errors) may cause additional coherence loss.

406

References

407 Abramowitz, M., and I. Stagun (1965), *Handbook of Mathematical Functions*, Dover,
408 New York.

409 Antony, J. W., J. Hueso González, M. Schwerdt, M. Bachmann, G. Krieger, and
410 M. Zink (2013), Results of the TanDEM-X baseline calibration, *IEEE J. of Sel.*
411 *Topics Appl. Earth Observ.*, *6*, 1495–1501.

412 Bachmann, M., and H. Hoffmann (2010), Challenges of the TanDEM-X commission-
413 ing phase, *Proc. EuSAR*, Aachen, Germany.

414 Bachmann, M., D. Schulze, C. Ortega-Míguez, D. Polimeni, J. Böer, J. Hueso
415 González, J. W. Antony, G. Krieger, B. Bräutigam, M. Schwerdt, and M. Zink
416 (2012), TanDEM-X acquisition status and calibration of the interferometric sys-
417 tem, *Proc. IGARSS*, Munich, Germany, 1900–1903.

418 Bamler, R., and P. Hartl (1998), Synthetic aperture radar interferometry, *Inv. Prob.*,
419 *14*, R1–R54.

420 Borla Tridon, D., M. Bachmann, D. Schulze, C. Ortega-Míguez, M. D. Polimeni,
421 and M. Martone (2013), TanDEM-X: DEM acquisition in the third year era, *Proc.*
422 *SFFMT*.

423 Buckreuss, S., and B. Schättler (2010), The TerraSAR-X ground segment, *IEEE*
424 *Trans. Geosci. Remote Sens.*, *48*(2), 623–632.

425 Farr, T. G., P. A. Rosen, E. Caro, R. Crippen, R. Duren, S. Hensley, M. Kobrick,
426 M. Paller, E. Rodriguez, L. Roth, D. Seal, S. Shaffer, J. Shimada, J. Umland,
427 M. Werner, M. Oskin, D. Burbank, and D. Alsdorf (2007), The Shuttle Radar
428 Topography Mission, *Rev. Geophys.*, *45*, RG2004, doi:10.1029/2005RG000183.

429 Fritz, T., C. Rossi, N. Yague-Martinez, F. Rodriguez-Gonzalez, M. Lachaise, and
430 H. Breit (2011), Interferometric Processing of TanDEM-X data, *Proc. IGARSS*,
431 Vancouver, Canada, 2428–2431.

432 Gatelli, F., A. M. Guarnieri, F. Parizzi, P. Pasquali, C. Prati, and F. Rocca (1994),
433 The wavenumber shift in SAR interferometry, *IEEE Trans. Geosci. Remote Sens.*,
434 *32*(4), 855–865.

435 European Space Agency GLOBCOVER. http://ionia1.esrin.esa.int/ (accessed 02.12).

436 Gruber, A., B. Wessel, M. Huber, and A. Roth (2012), Operational TanDEM-X
437 DEM calibration and first validation results, *ISPRS J. of Photogr. Remote Sens.*,
438 *73*, 39–49.

439 Huber, M., A. Gruber, A. Wendleder, B. Wessel, A. Roth, and A. Schmitt (2007),
440 The global TanDEM-X DEM: production status and first validation results, *Proc.*
441 *XXII ISPRS Congress*, Melbourne (Australia), 45–50.

442 Hueso González, J., M. Bachmann, and H. Hoffmann (2010), TanDEM-X commis-
443 sioning phase status, *Proc. IGARSS*, Honolulu, Hawaii, 2633–2635.

444 Hueso González, J., J. W. Antony, M. Bachmann, G. Krieger, M. Schwerdt, and
445 M. Zink (2012), Tests of the TanDEM-X DEM calibration performance, *Proc.*
446 *IGARSS*, Munich, Germany, 303–306.

Hueso González, J., J. W. Antony, M. Bachmann, G. Krieger, M. Zink, D. Schrank, and M. Schwerdt (2012), Bistatic system and baseline calibration in TanDEM-X to ensure the global digital elevation model quality, *ISPRS J. of Photogr. Remote Sens.*, *73*, 3–11.

Just, D., and R. Bamler (1994), Phase statistics of interferograms with applications to synthetic aperture radar, *Applied Optics*, *33*(20), 4361–4368.

Kraus, T., D. Schrank, P. Rizzoli, and B. Bräutigam (2011), In-orbit performance of TerraSAR-X and TanDEM-X satellites, *URSI-F-Triennal Symposium*, Garmisch-Partenkirchen, Germany.

Krieger, G., A. Moreira, H. Fiedler, I. Hajnsek, M. Werner, M. Younis, and M. Zink (2007), TanDEM-X: a satellite formation for high-resolution SAR interferometry, *IEEE Trans. Geosci. Remote Sens.*, *45*(11), 3317–3341.

Kwok, R., and W. T. K. Johnson (1989), Block Adaptive Quantization of Magellan SAR data, *IEEE Trans. Geosci. Remote Sens. Lett.*, *27*(4), 375–383.

Lachaise, M., M. Eineder, and T. Fritz (2007), Multi baseline SAR acquisition concepts and phase unwrapping algorithms for the TanDEM-X mission, *Proc. IGARSS*, Barcelona (Spain), 5272–5276.

Lachaise, M., U. Balss, T. Fritz, and H. Breit (2012), The dual-baseline interferometric processing chain for the TanDEM-X mission, *Proc. IGARSS*, Munich (Germany), 5562–5565.

Lancashire, D. C., B. A. F. Barnes, and S. J. Udall (1999), Block adaptive quantization, *US Patent*, http://www.patentlens.net/patentlens/patent/US6255987/.

Lee, J.-S., K. W. Hoppel, S. A. Mango, and A. R. Miller (1994), Intensity and phase statistics of multilook polarimetric and interferometric SAR imagery, *IEEE Trans. Geosci. Remote Sens.*, *32*(5), 1017–1028.

Li, F. K., and R. M. Goldstein (1990), Studies of multibaseline spaceborne interferometric synthetic aperture radars, *IEEE Trans. Geosci. Remote Sens.*, *28*(1), 88–97.

Martone, M., B. Bräutigam, P. Rizzoli, C. Gonzalez, M. Bachmann, and G. Krieger (2012), Coherence evaluation of TanDEM-X interferometric data, *ISPRS J. of Photogr. Remote Sens.*, *73*, 21–29.

Martone, M., B. Bräutigam, and G. Krieger (2012), Decorrelation effects in bistatic TanDEM-X data, *Proc. IGARSS*, Munich, Germany, 5558–5561.

Mittermayer, J., M. Younis, R. Metzig, S. Wollstadt, J. M. Martinez, and A. Meta (2010), TerraSAR-X system performance characterization and verification, *IEEE Trans. Geosci. Remote Sens.*, *48*(2), 660–676.

Moreira, A., G. Krieger, I. Hajnsek, M. Werner, D. Hounam, and S. Riegger (2004), TanDEM-X: a TerraSAR-X add-on satellite for single-pass SAR interferometry, *Proc. IGARSS*, Anchorage, Alaska (USA), 1000–1003.

Ortega-Míguez, C., D. Schulze, M. D. Polimeni, P. Rizzoli, and M. Bachmann (2012), TanDEM-X acquisition planner, *in EuSAR*, Nuremberg, Germany.

Rizzoli, P., B. Bräutigam, T. Kraus, M. Martone, and G. Krieger (2012), Relative height error analysis of TanDEM-X elevation data, *ISPRS J. of Photogr. Remote Sens.*, *73*, 30–38.

491 Rizzoli, P., M. Bachmann, and B. Bräutigam (2012), Global performance monitoring
492 from TanDEM-X quicklook data, *Proc. EuSAR*, Nuremberg, Germany.
493 Rodriguez, E., C. H. Morris, and J. E. Belz (2006), A global assessment of the SRTM
494 performance, *Photogr. Eng. and Remote Sens.*, *72*(3), 249–260.
495 Rossi, C., R. Rodriguez Gonzalez, T. Fritz, N. Yague Martinez, and M. Eineder
496 (2012), TanDEM-X calibrated Raw DEM generation, *ISPRS J. of Photogr. Remote*
497 *Sens.*, *73*, 12–20.
498 Suchandt, S., and M. Eineder (2003), Experiences with STRM/X-SAR phase un-
499 wrapping using the minimum cost flow method, *Proc. IGARSS*, Toulouse, France,
500 4380–4382.
501 Schwerdt, M., D. Schrank, M. Bachmann, J. Hueso González, B. Döring, N. Tous Ra-
502 mon, and J. W. Antony (2012), Calibration of the TerraSAR-X and the TanDEM-X
503 satellite for the TerraSAR-X mission, *Proc. EuSAR*, Nuremberg, Germany, 56–59.
504 TanDEM-X Science Server System. https://tandemx-science.dlr.de/ (accessed 05.10).
505 Treuhaft, R. N., and P. R. Siqueira (2000), Vertical structure of vegetated land
506 surfaces from interferometric and polarimetric radar, *Radio Sci.*, *35*(1), 141–177.
507 Werninghaus, R., and S. Buckreuss (2010), The TerraSAR-X mission and system
508 design, *IEEE Trans. Geosci. Remote Sens.*, *48*(2), 606–614.
509 Wessel, B. (2013), TanDEM-X Ground Segment - DEM products specification doc-
510 ument, TD-GS-PS-0021 (2.0), 22.04.2013.
511 Zebker, H. A., and J. Villasenor (1992), Decorrelation in interferometric radar echoes,
512 *IEEE Trans. Geosci. Remote Sens.*, *30*(5), 950–959.

513 Zebker, H. A., T. G. Farr, R. P. Salazar, and T. H. Dixon (1994), Mapping the world's
514 topography using radar interferometry: the TOPSAT mission, *Proc. IEEE*, *82*(12),
515 1774–1786.

516 Zebker, H. A., and Y. Lu (1998), Phase unwrapping algorithms for radar interfer-
517 ometry: residue-cut, least-squares, and synthesis algorithms, *J. Opt. Soc. Am. A.*
518 *Opt. Image Sci. Vis.*, *15*(3), 586–598.

Table 1. Comparison of SRTM and TanDEM-X DEM specifications.

Requirement	Specification	SRTM	TanDEM-X
Relative Vertical Accuracy	90% linear point-to-point error over a 1° x 1° cell	12 m (slope < 20%) 15 m (slope > 20%)	2 m (slope < 20%) 4 m (slope > 20%)
Absolute Vertical Accuracy	90% linear error	18 m	10 m
Absolute Horizontal Accuracy	90% circular error	23 m	10 m
Spatial Resolution	independent pixels	30 m (1 arc sec at equator)	12 m (0.4 arc sec at equator)

Table 2. Acquisition parameters and mean performance for two repeated data-takes over Death Valley (RHE: relative height error). A good agreement with the height error estimated from repeated DEM acquisitions has been verified (see Figure 4: 90% p-to-p RHE of about 2.3 m).

Acq. Date	Polarization	HoA ($B_\perp$)	Inc. Angle	Mean Coherence	90% p-to-p RHE from Coherence
2011-04-07	HH	38.8 m (172 m)	40.7°	0.811	2.22 m
2011-04-18	HH	39.3 m (170 m)	40.7°	0.806	2.25 m

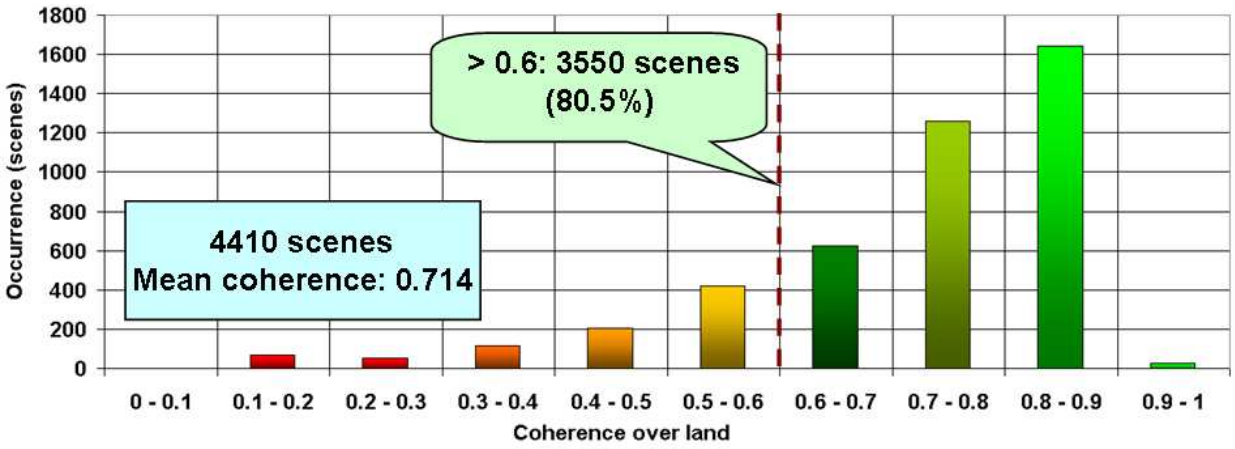

Figure 1. Interferometric coherence of test acquisitions during the TanDEM-X bistatic commissioning phase. For each scene, the mean coherence over land is considered.

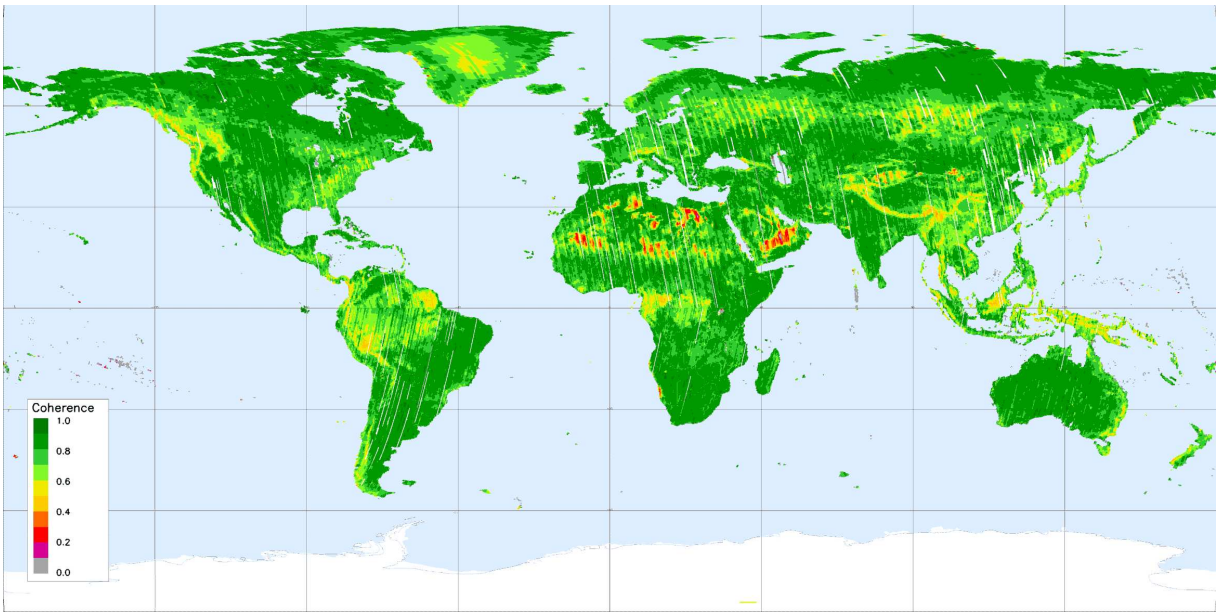

Figure 2. Coherence distribution of the first TanDEM-X global DEM acquisitions.

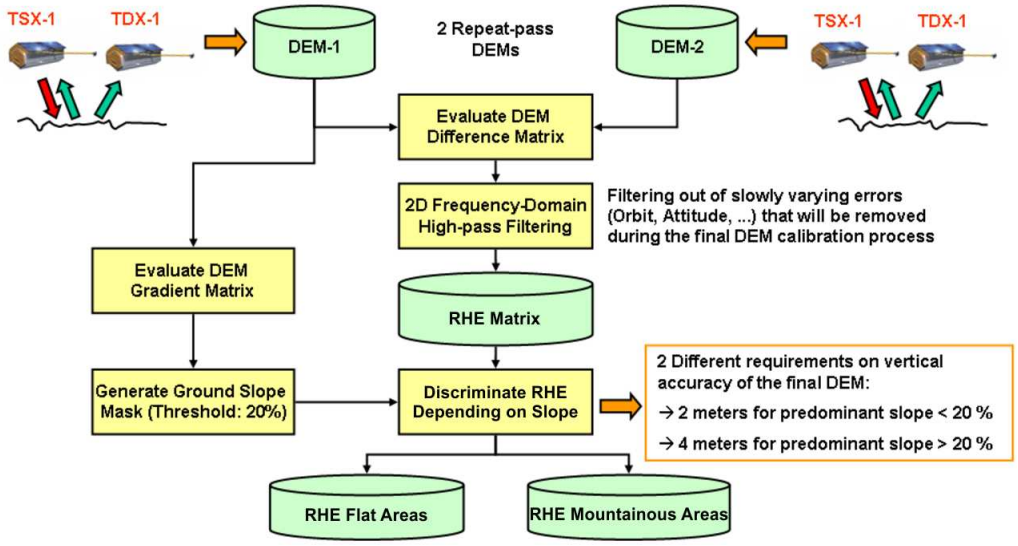

Figure 3. Relative height error (RHE) analysis workflow for repeat-pass DEMs.

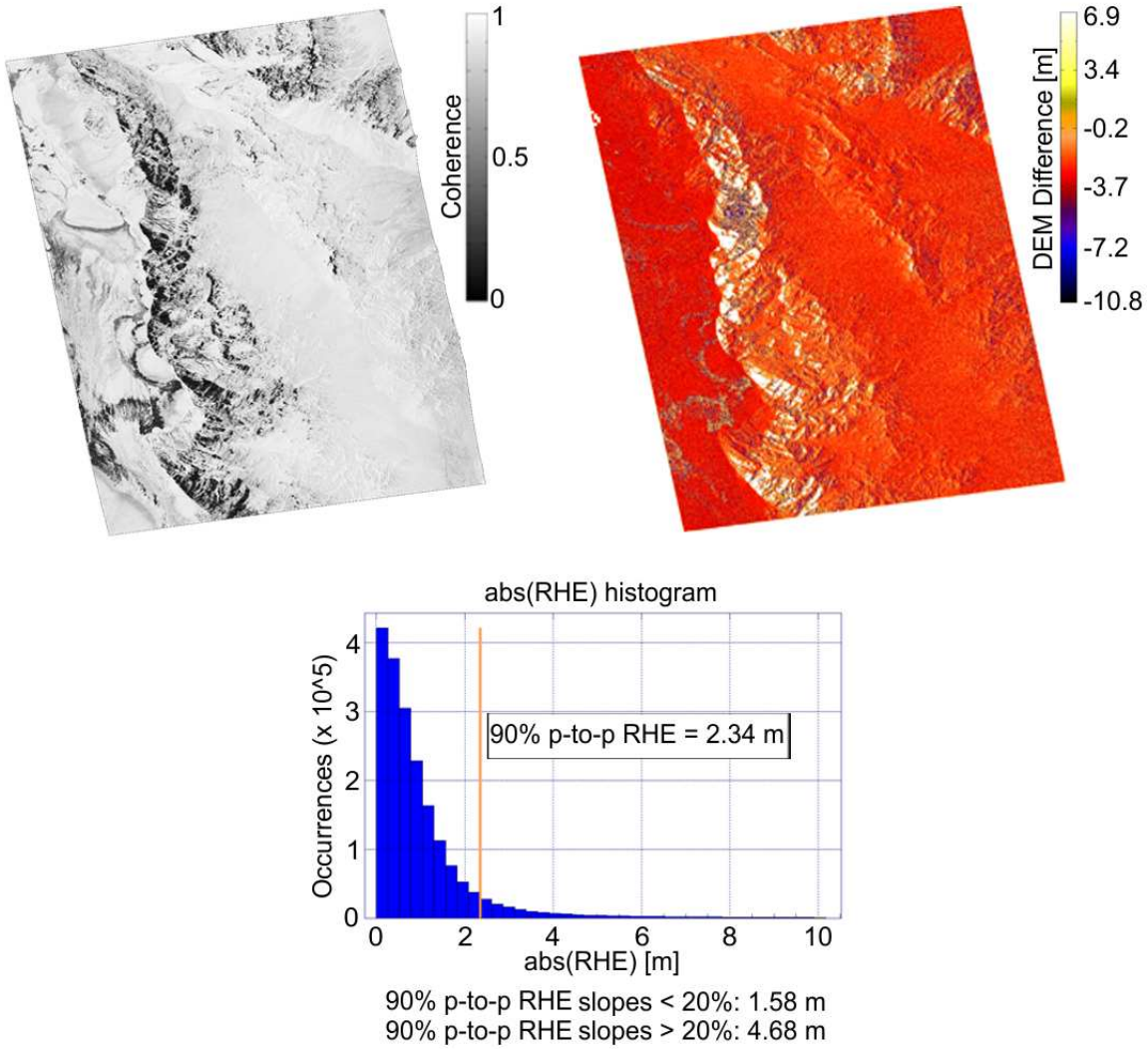

Figure 4. (Top-left) Coherence map over an area located in Death Valley (USA), which has been investigated for relative height error verification. (Top-right) DEM difference between two repeated acquisitions. (Bottom) Histogram for the point-to-point relative height error (p-to-p RHE). The 90% values obtained for flat and mountainous areas are indicated below the figure.

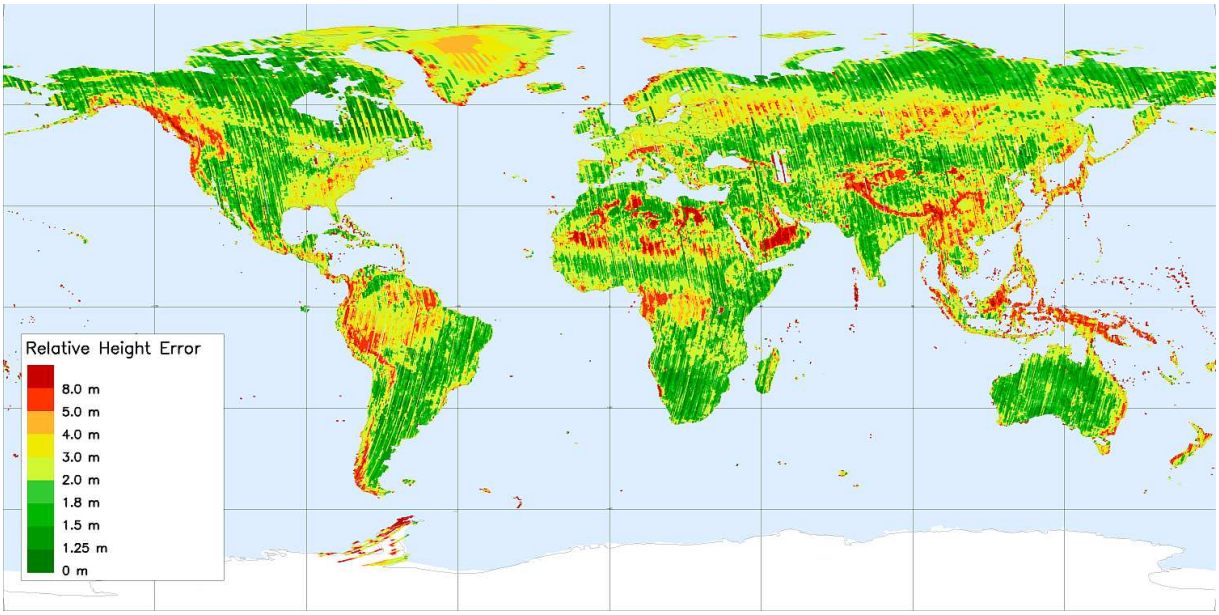

Figure 5. 90% point-to-point relative height error distribution of the first TanDEM-X global DEM coverage, estimated from the mean coherence value per bistatic scene. For the regions depicted in green a single acquisition is already fulfilling the 2 m specification. Areas represented in yellow and red require multiple interferometric acquisitions in order to improve the overall performance.

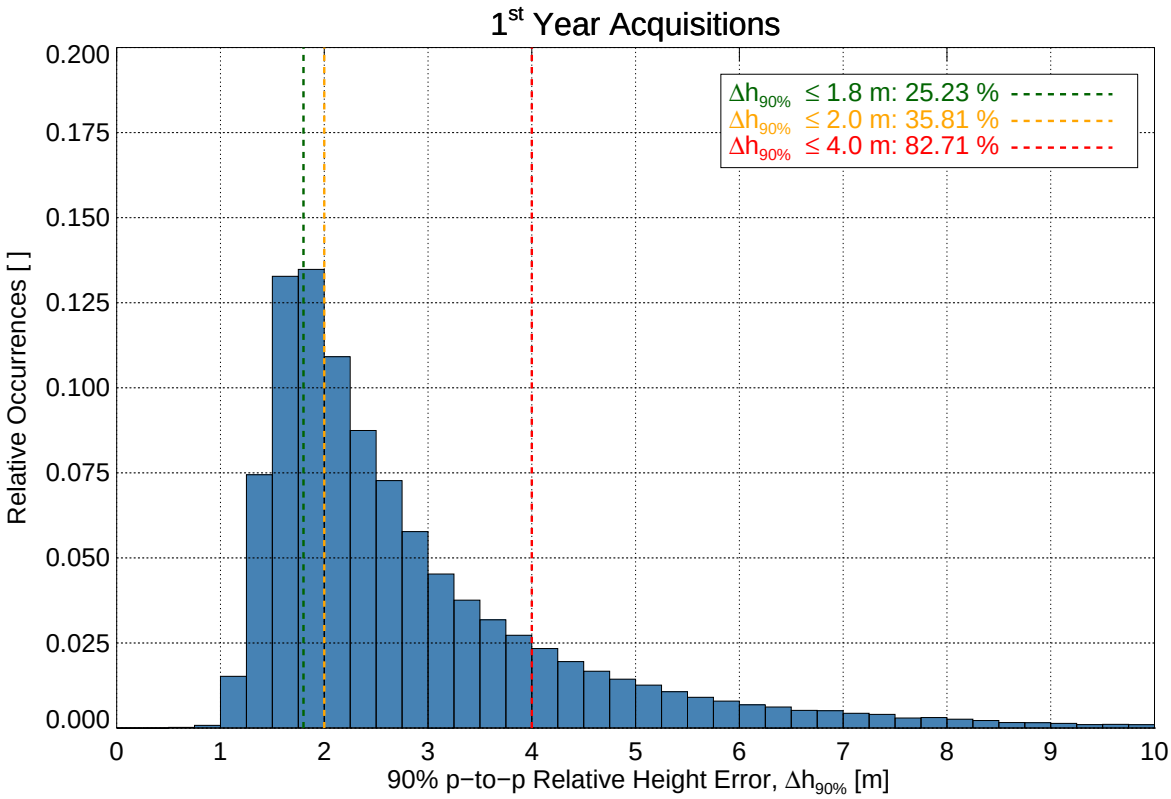

Figure 6. Histogram for the 90% point-to-point relative height error of the first TanDEM-X global DEM acquisitions (in total, about 120,000 scenes). The legend and the vertical dashed lines indicate the percentage of scenes showing a 90% point-to-point relative height error below 1.8 m, 2.0 m and 4.0 m.

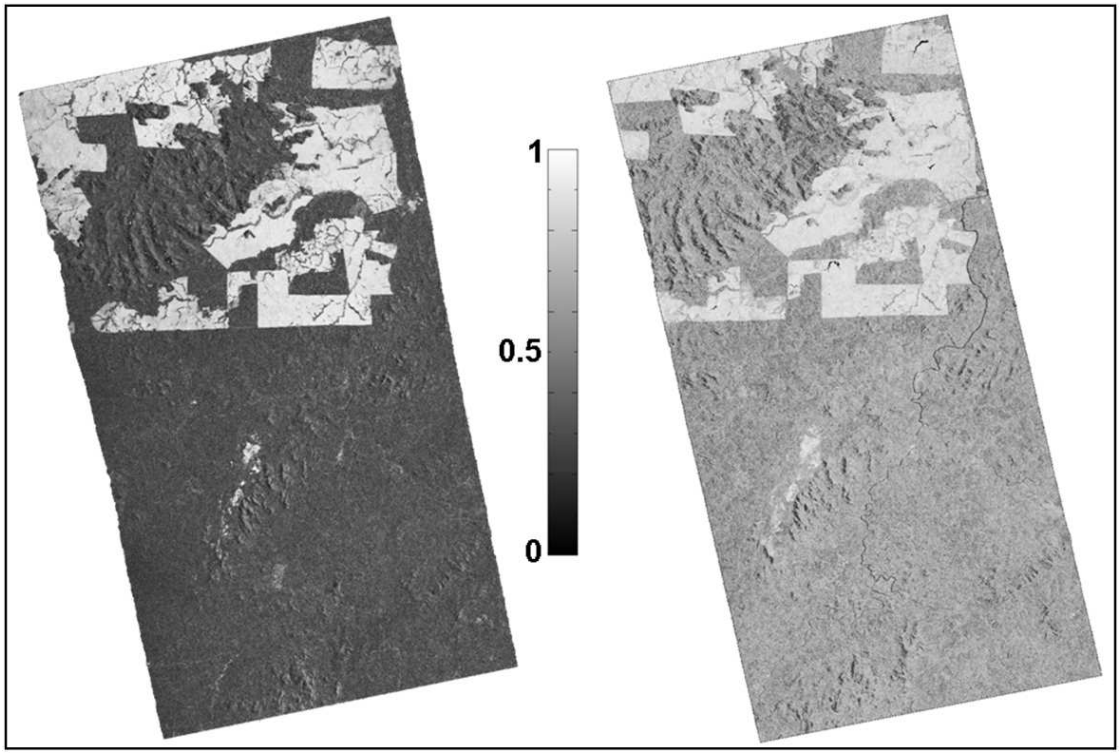

Figure 7. Coherence maps over the Amazon rainforest. (Left) HH polarization, HoA: 25 m ($B_\perp$: 182 m), θ_{inc}: 29.9°, mean coherence over the forest ~ 0.3. (Right) HH polarization, HoA: 52 m ($B_\perp$: 162 m), θ_{inc}: 47.7°, mean coherence over the forest ~ 0.6. In the clear-cut areas, the mean coherence is ~ 0.8 for both images.

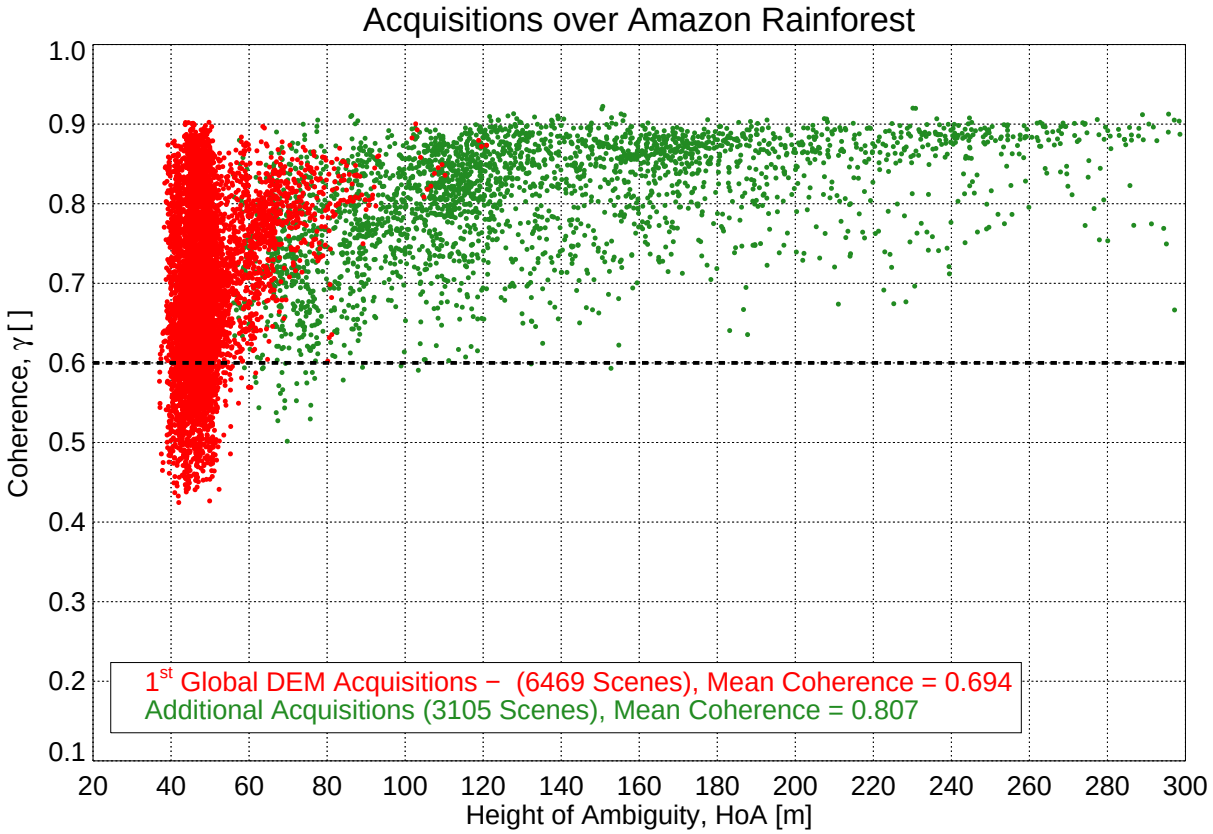

Figure 8. Coherence against height of ambiguity for acquisitions performed during nominal DEM phase over the Amazon rainforest. Acquisitions from the first global DEM are plotted in red (the HoA ranges typically between 40 and 50 m). Additional acquisitions over densely forested areas have been performed with smaller baselines (depicted in green), in order to improve performance and unwrapping quality. For height of ambiguities greater than 55 m, coherence is usually above 0.6, and a mean improvement with respect to the first global DEM acquisitions of about 16% has been obtained.

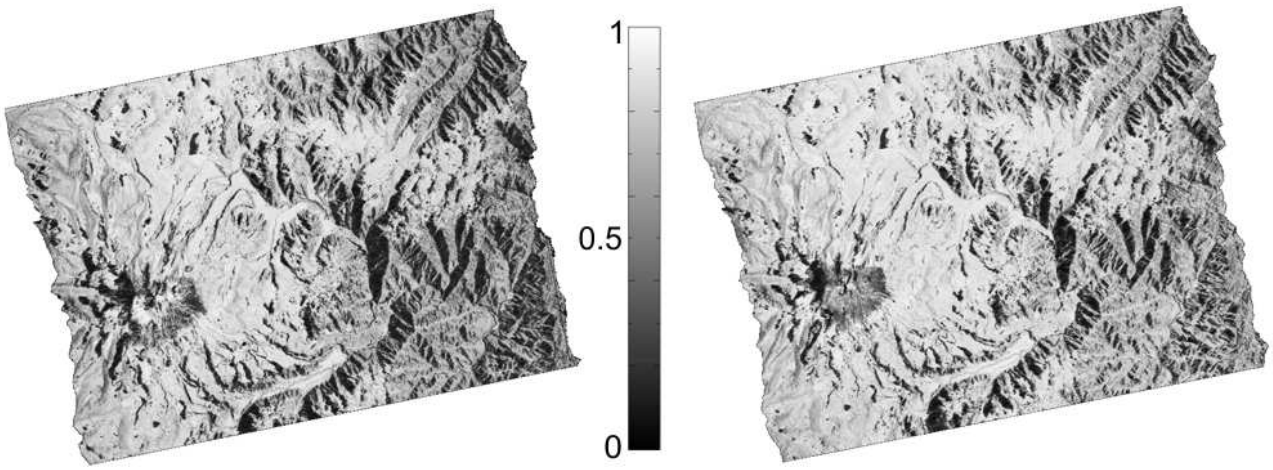

Figure 9. Coherence maps for two acquisitions over the Cayambe volcano (Ecuador). (Left) HH polarization, HoA: 48 m ($B_\perp$: 120 m), θ_{inc}: 36.1°, mean coherence is $\sim$ 0.62. (Right) HH polarization, HoA: 77 m ($B_\perp$: 76 m), θ_{inc}: 36.1°, mean coherence is $\sim$ 0.68.

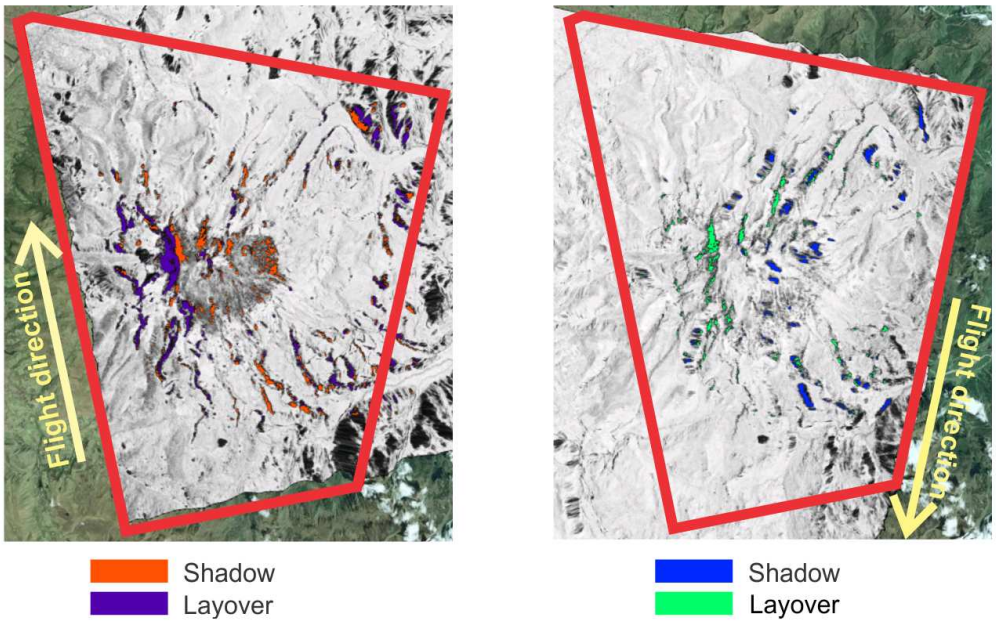

Figure 10. Shadow/layover and coherence for two acquisitions over the Cayambe volcano (Ecuador). (Left) Ascending orbit direction, HH polarization, HoA: 77 m ($B_{\perp}$: 76 m), θ_{inc}: 36.1°, shadow and layover are represented with orange and violet color, respectively. (Right) Descending orbit direction, HH polarization, HoA: 286 m ($B_{\perp}$: 26 m), θ_{inc}: 40.6°, shadow and layover are depicted in blue and green, respectively. The overlapping area between the two images is outlined in red.

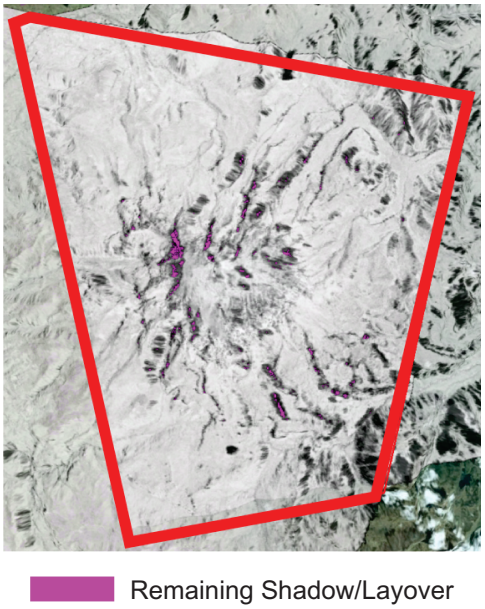

Figure 11. Remaining shadow/layover after combination of the two acquisitions shown in Figure 8 (depicted in pink), which correspond to the pixels where both images are affected. More than 70% of shadow/layover present in the ascending orbit and more than 50% of shadow/layover present in the descending orbit acquisition could be resolved.

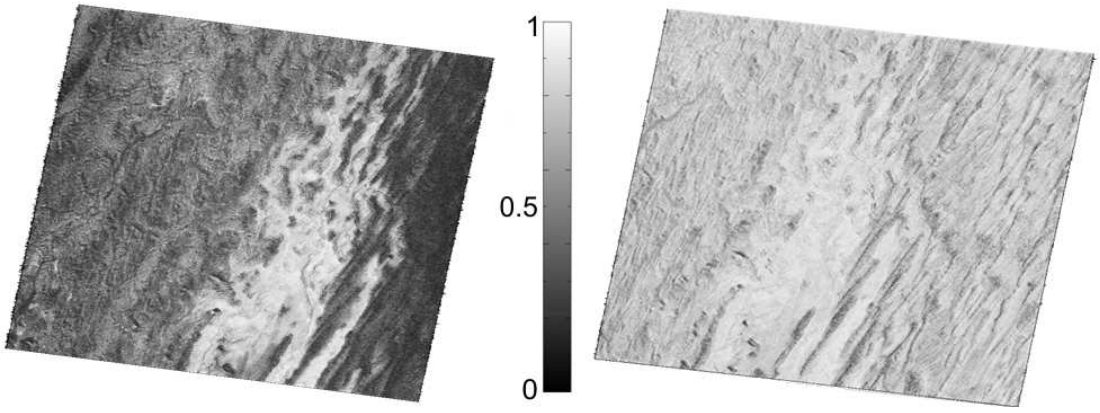

Figure 12. Coherence maps over an area located in the Taklamakan desert; (left) HoA: 442 m ($B_\perp$: 16.7 m), θ_i: 42.6°, mean coherence over sand ~ 0.44; (right) HoA: 140 m ($B_\perp$: 28.9 m), θ_i: 26.3°, mean coherence over sand ~ 0.71. In the rocky area, the mean coherence is ~ 0.8 for both images.

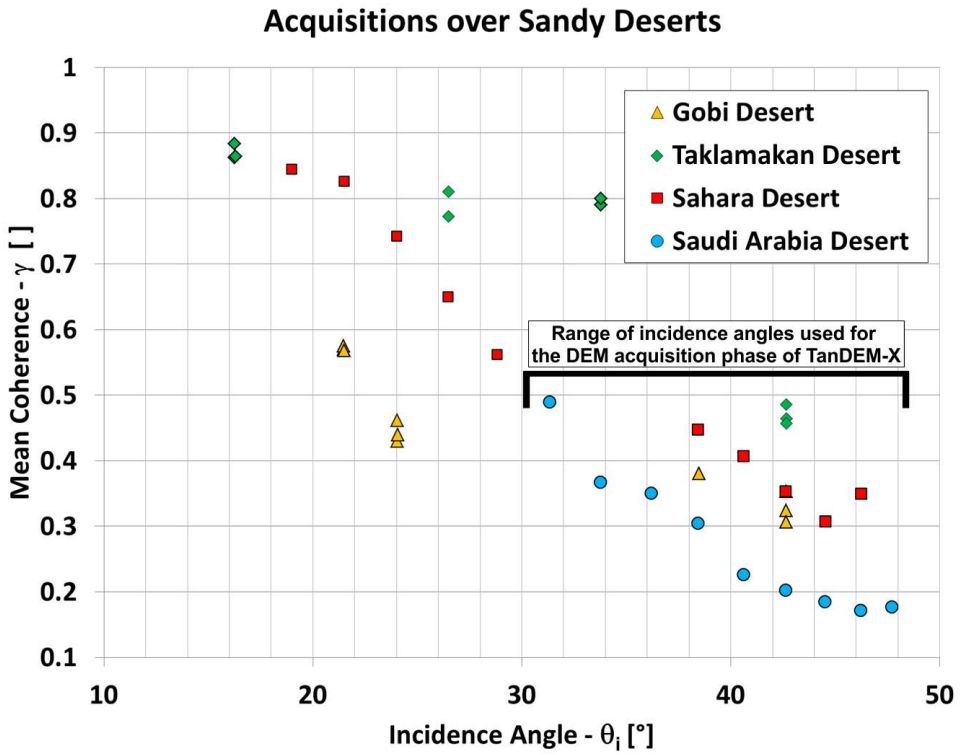

Figure 13. Dependence of SNR decorrelation on the incidence angle for different desert areas.